The role of surface spin polarization on ceria-supported Pt nanoparticles

Byungkyun Kang,[1] Joshua L.Vincent,[2] Peter A. Crozier,[2] and Qiang Zhu[1]
[1)]*Department of Physics and Astronomy, University of Nevada, Las Vegas, NV 89154, USA*
[2)]*School for Engineering of Matter, Transport, and Energy, Arizona State University, Tempe, AZ 85281, USA*

(Dated: 5 October 2021)

In this work, we employ first-principles simulations to investigate the spin polarization of CeO_2-(111) surface and its impact on interactions between a ceria support and Pt nanoparticles. For the first time, we report that the CeO_2-(111) surface exhibits a robust surface spin polarization due to the internal charge transfer between atomic Ce and O layers. In turn, it can lower the surface oxygen vacancy formation energy and enhance the oxide reducibility. We show that the inclusion of spin polarization can therefore significantly reduce the major activation barrier in the proposed reaction pathway of CO oxidation on ceria-supported Pt nanoparticles. For metal-support interactions, surface spin polarization enhances the bonding between Pt nanoparticle and ceria surface oxygen, while CO adsorption on Pt nanoparticles weakens the interfacial interaction regardless of spin polarization.

I. INTRODUCTION

In heterogeneous catalysis, metal nanoparticles supported on reducible oxide structures provide unique interfacial interactions which lead to the formation of active sites at the three-phase boundaries which control activity and selectivity for oxidation reactions[1,2]. Many high-performance heterogeneous catalysts have been developed which exploit the metal/oxide interface properties for reactions such as CO oxidation at room and low temperature[3–6]. The ability of reducible oxides to donate lattice oxygen during a reaction (the so-called Mars van Krevellen mechanism) was first described nearly 70 years ago and is now an accepted kinetic pathway for many reactions[7]. The atomic level details of how such a mechanism operates especially in the presence of metallic nanoparticles remains poorly understood. Tauster was one of the first to recognize the unique properties of the metal-support interaction (MSI) with his observation of metal nanoparticles being encapsulated with thin overlayers under strong reducing condition[8–10]. The strong MSI has been realized in redox transition metal oxides[8–11] and even a relatively redox-inert alkaline metal oxide MgO[12]. The MSI is also associated with occurrence of charge transfer at the interface[13]. Campbell proposed the electronic MSI mechanism, in which charge transfer at the metal/oxide interface modulates chemical activity of the supported catalyst[14]. The electronic MSI gives rise to a rearrangement of electrons within the interface and enhances the rate of surface oxygen vacancy creation/annihilation leading to an enhanced catalytic activity[15].

To manipulate the role of the interfacial interactions on a catalytic reaction, the nanoparticle size can be varied to change the contact area between the metal and support interface[16]. For Au/Co_3O_4 and Au/Fe_2O_3, the gold nanoparticles with a diameter smaller than 5 nm show high reaction activity[17] and Pt particles of 2-3 nm were found to be more active for CO oxidation[18]. In the limiting case, the metal nanoparticles may be reduced all the way down to a single atom, giving rise to the so-called single atom catalysts[19]. Another approach to manipulate catalytic activity is by tuning the interfacial interaction directly. This has been realized by varying the support type, particles shape and size. The aforementioned nanostructuring creates new metal-support interaction resulting in the metal nanoparticle properties being substantially different from their bulk counterparts[16]. Doping oxides by heteroatoms can modify the electronic structure. They enhance surface oxygen reducibility by tuning the interfacial interaction[20]. The increased oxide reducibility linked to surface oxygen vacancy formation energy is an indispensable element in oxidation reactions based on the Mars-van Krevelen mechanism[20–25]. In combination with the smaller nanoparticles, nano-structured oxide supports further lower the surface oxygen vacancy formation energy and gives rise to a reverse spillover of the surface oxygen on to the Pt nanoparticle[26]. These works highlight the importance of undertaking fundamental studies to elucidate the complex interfacial interaction underlying catalytic functionality.

There remain a paucity of information about the atomic structure and structural dynamics of an active metal-support interface performing catalysis. Recently, there has been an emerging paradigm that has roots in surface science[27–29] and chemistry[30] for understanding catalytically active sites in terms of dynamic, meta-stable, or so-called fluxional species from both computation[31–33] and experimental work[34–36]. This has raised many questions regarding both the fundamental structure of active sites and the atomic scale evolution of the interface, metal particle, and adjacent oxide surface during catalysis. For example, what is the dynamic nature of the metal-support interface? The adhesion between the metal particle and support may weaken significantly since bridging oxygen are responsible for anchoring the metal to the support. How does the metal-support interface change in the presence of reactant adsorbates and reaction intermediates? How do such structural changes impact activation of intermediates and facilitate the bond breaking and formation along the reaction pathways? What happens during the rate limiting step and where is the likely site for CO_2 formation and desorption. In order to deepen our understanding of the factors affecting catalysis and to develop strategies for improved catalyst design, it is essential to elucidate and describe the structural evolution that occurs at the atomic level during simultaneous catalytic turnover.

In this work, we investigated the interfacial interaction of ceria-supported Pt nanoparticles by density functional theory (DFT) simulations. We found that spins are polarized on the CeO_2-(111) surface through charge transfer from surface oxygen to cerium, which can significantly lower the oxygen vacancy formation energy and alter the interfacial interaction between Pt nanoparticle and ceria support. In turn, the activated surface plays an essential role in lowering the major activation barrier in the proposed reaction pathway of CO oxidation on the ceria-supported Pt nanoparticles. Using the existence of a robust surface spin polarization, we propose a theoretical description of the recently observed controversial room temperature magnetism in ceria nanostructures[37].

II. COMPUTATIONAL METHODS

We used the slab model with five O-Ce-O layers to simulate the CeO_2-(111) surface with a 6×6 reconstruction of the primitive unitcell. Experimental lattice constants (a=b=5.410 Å)[38] of ceria with 15 Å vacuum along the z direction have been used throughout. To make Pt(111) interface with CeO_2-(111), a hexagonal Pt_{19} single layer (SL) was built. As initial structure for geometry optimization, we have located the center of Pt_{19} SL 2.5 Å above oxygen on the CeO_2-(111) surface, while Pt_{19} SL [100] and CeO_2 [110] are coincided. This model was relaxed at the level of DFT by using the CP2K package[39]. In CP2K, the wavefunction was expanded in the double ζ valence plus polarization and plane-wave basis sets with an energy cutoff of 400 Ry. We used Geodecker-Teter-Hutter pseudopotentials[40] based on the GGA[41] functional. The van der Waals interaction was also considered according to the DFT-D3 scheme[42]. For all spin polarized calculations, half spin moments on Pt and Ce atoms were given as the initial guess. To account for the strongly correlated nature of Ce's $4f$ electrons, we employed the DFT+U method with U = 7 eV, as suggested by the previous studies [43,44]. To check the effect of U, we also repeated some representative calculations using U = 4 eV. The climbing image-nudged elastic band (CI-NEB) method [45] was used to simulate the activation barriers for the proposed reaction pathway of CO oxidation on the ceria-supported Pt nanoparticles. To find surface spin polarization effect on the lattice dynamic reconfiguration, we performed the *ab-initio* molecular dynamic (AIMD) simulation at 300 K with 1 fs time step using Nose-Hover thermostat. To prevent high computational cost, only three layers of O-Ce-O were considered in the AIMD simulation. In all simulations, the atoms on the lowest O-Ce-O layer were kept fixed.

From the aforementioned DFT simulations, we obtained the adsorption energy using the following equation:

$$E_{\text{ads}} = E_{(\text{slab\_adsorbate})} - E_{\text{slab}} - E_{\text{adsorbate}} \quad (1)$$

where $E_{(\text{slab\_adsorbate})}$ is the energy of optimized slab model with adsorbates, E_{slab} is the energy of pure surface slab, and $E_{\text{adsorbate}}$ is the energy of adsorbate, respectively.

Oxygen vacancy formation energy is

$$E^{\text{F}}_{\text{Vo}} = E_{(\text{slab\_Vo})} - E_{\text{slab}} + 1/2E_{\text{O}_2} \quad (2)$$

where E_{O_2} is the total energy of the ground (triplet) state of oxygen molecule in the gas phase.

Surface energy of slab is defined by

$$E_{\text{surf}} = (E_{\text{slab}} - nE_{\text{bulk}})/(2S) \quad (3)$$

where n is the number of formula unit in the slab, and S is the surface area.

III. RESULT AND DISCUSSIONS

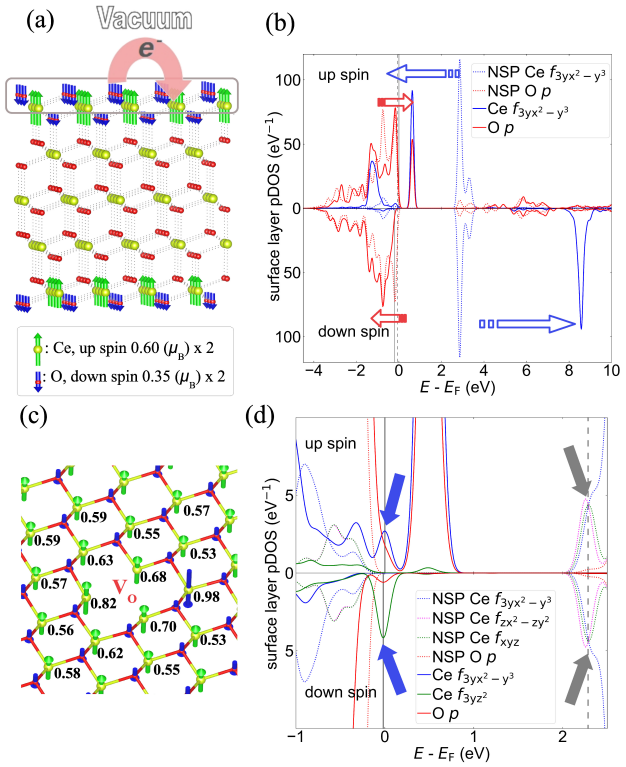

FIG. 1. Calculated surface spin polarization and surface oxygen vacancy. (a) Optimized CeO_2-(111) surface. Green (blue) vector denotes calculated Mulliken up (down) spin population multiplied by scale factor 2.0 for visualizing the moment (Note that the same scale factor is used for all figures in this work). For clarity, only the spin population larger than 0.20 μ_B is shown here. The lower inset shows the scale of vectors. (b) Calculated surface layer projected density of state. The density of state of upper oxygen and cerium layers marked by grey box in (a) are shown. The blue (red) arrows denote the relative shifts of Ce-f (O-p) states between SP and NSP simulations. (c) Optimized surface geometry with oxygen vacancy. (d) Calculated surface layer projected density of state for the oxygen vacancy configuration. The blue (gray) arrows point to defect states obtained from SP (NSP) simulation. In (c) and (d), the zero of energy set to chemical potential of up spin from spin polarized simulation, and relative chemical potentials are marked by solid (dashed) vertical lines for SP (NSP) simulation.

A. Surface spin polarization

We first performed the geometry optimization with initial magnetic moment on all cerium atoms to include surface spin polarization explicitly. Fig. 1a shows the optimized CeO_2-(111) surface where spins are polarized. The average Mulliken spin moment per atom is 0.60 (-0.35) μ_B on the uppermost cerium (oxygen) layer. This structure contains spin polarization on both top and bottom O-Ce-O surface layers. The spin polarization in the bottom layer (with frozen atoms) is weaker than that in the upper layer (with free atoms), indicating a Jahn-Teller effect [46–49]. Fig. 1b shows the projected density of states (DOS) of surface layers. For a comparison, the DOS without spin polarization is also shown here. The spin polarized DOS near the Fermi energy is comprised of appreciable hybridization between Ce-f and O-p orbitals. The occupied (unoccupied) up spin states derived by bonding (antibonding) of Ce-f and O-p characters form the narrow bands. The exchange splitting is explained by comprehensive comparison of spin polarized (SP) and non-spin polarized (NSP) DOS. Compared to the NSP system, the Ce-f states were split into the unoccupied down spin states and occupied up spin state (see the blue arrows in Fig. 1b). In consequence, the net up spin moment is populated on surface cerium atoms. On the other hand, the original O-p states (from NSP calculation) were pushed up into unoccupied state in up spin and pushed down into lower energy states in down spin (see the red arrows in Fig. 1b), resulting a population of the net down spin moment on surface oxygen atoms.

Compared to the NSP calculation, the inclusion of spin polarization lowers the total energy by 7.83 eV. The energy drop is derived by just outermost two O-Ce-O layers (surface layers) where spins are polarized, since there is no sizeable spin polarization on other layers. Accordingly, the energy gain corresponds to 3.92 eV per surface layer or 0.11 eV per O-Ce-O in the surface layer (there are 36 O-Ce-O units in the surface layer). One can confirm that this estimation is appropriate based on constant total energy difference between SP and NSP systems with respect to number of layers, as shown in Table. I. This significant energy difference indicates the existence of a strong spin polarization on CeO_2-(111) surface. We did not find any antiferromagnetic configuration in this system. Therefore, we conclude that the CeO_2-(111) surface is ferromagnetic.

While the room temperature magnetism in CeO_2 has been studied extensively, its origin remains unclear[37]. Here, we propose a new theoretical description of the room temperature ferromagnetism in undoped ceria nanostructure[50–56] and thin films[57–61]. It was suggested that the ferromagnetism is confined to the ceria nanostructure surface where oxygen vacancy may play an important role[53,54,57]. On the contrary, Li *et al.*[51] and Liu *et al.*[55] proposed that the ferromagnetism does not relate to the surface oxygen vacancy but to the surface Ce^{3+}/Ce^{4+} pairs. A number of DFT studies have attributed the ferromagnetism to native defects such as oxygen vacancy. The defect formation causes spin polarization of f electrons for Ce ions near the vacancy, resulting in a nonzero net magnetic moment on the ceria surface[59,62–67]. Nevertheless, based on our results, the ferromagnetism may emerge in a bare surface without any defect or impurity. In general, it was perceived that ions on the surface with lower coordination numbers can cause an unusual spin population [68–70]. In our case, vacuum acts as a virtual doping on the surface: hole doping for oxygen layer lowering the chemical potential of surface oxygen and electron doping for cerium layer. Upon significant spin exchange interaction on the surface, the virtual doping leads to a charge transfer from oxygen layer to cerium layer, resulting in $Ce^{4+} \rightarrow Ce^{3+}$ transition and partially filled O-p on the surface layer (see Figure 1a-b). In consequence, the spin on ions couples ferromagnetically, which gains significant energy comparing to the NSP system. In addition, we emphasize that the charge transfer is fully triggered by the surface effect. As shown in Table I, increasing the number of layers reduces the surface/bulk ratio, resulting in an increased chemical potential which approaches to that of the bulk, while other quantities show no sizeable variation.

TABLE I. The slab size effect on surface spin polarization. The O1 (O2) denotes oxygen atoms on the top (bottom) layer within the surface O-Ce-O layer. The calculated quantities by surface spin polarized (SP) and non-spin polarized (NSP) simulations are presented. E_{surf} is the calculated surface energy. E_F^{bulk} and E_F^{slab} are the Fermi energies for ceria bulk and slab, respectively. E_{SP} and E_{NSP} are total energies of SP and NSP systems, respectively. $\{$O-Ce-O$\}_{surf}$ denotes O-Ce-O in the surface layer.

		Number of O-Ce-O layers				
		3	5	7	9	11
Spin population in surface layer (μ_B/atom)	Ce	0.55	0.60	0.58	0.56	0.56
	O1	-0.32	-0.35	-0.34	-0.33	-0.33
	O2	-0.19	-0.20	-0.20	-0.20	-0.20
E_{surf} (J/m^2)[a]	SP	0.94	0.94	0.95	0.95	0.96
	NSP	1.07	1.08	1.08	1.08	1.08
E_F^{bulk} - E_F^{slab} (eV)	SP	8.34	6.86	5.59	4.70	4.04
	NSP	8.44	6.93	5.64	4.77	4.12
E_{SP}-E_{NSP} (eV/$\{$O-Ce-O$\}_{surf}$)		-0.11	-0.11	-0.10	-0.10	-0.10

[a] Experimental surface energy is 1.2 ± 0.2 J/m^2 [71].

On account of the robust surface spin coupling, we investigated the impact of surface spin polarization on surface oxygen vacancy formation. Figure 1c-d show the optimized structure, spin population and DOS of surface layer with oxygen vacancy. In the SP simulation, the two excess electrons produced by the oxygen vacancy are populated on neighboring cerium atoms forming localized polaronic states. One electron was captured by three nearest neighboring Ce atoms, with the spin moments of 0.82, 0.68 and 0.70 μ_B, respectively. The other electron was localized on the next nearest neighboring Ce atom with 0.98 μ_B down spin moment having antiferromagnetic coupling with the surrounding Ce atoms (see Fig. 2a). The latter is associated with the increased local spin moment by Hund's rule within our singlet simulation. The oxygen vacancy defect states in the SP system are shallow, whereas the same defect states are below conduction band minimum in the NSP system. With this configuration, we

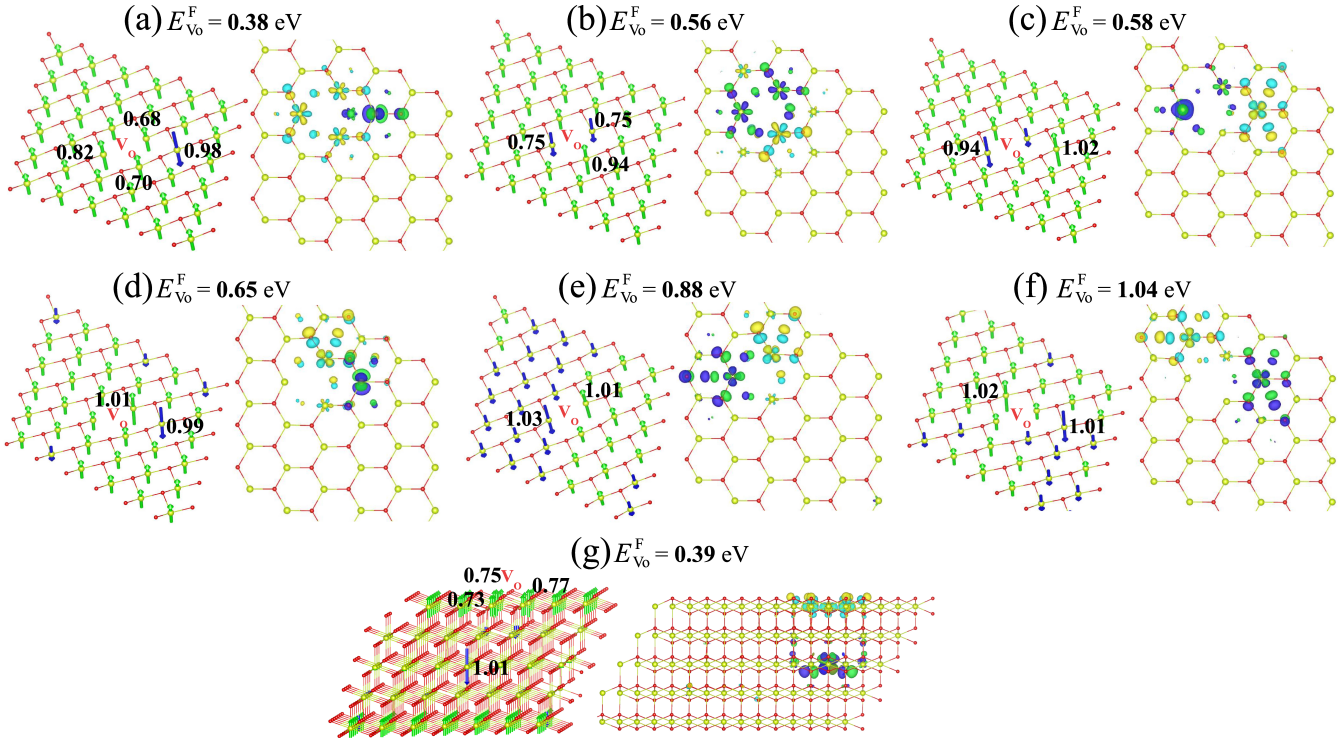

FIG. 2. Low-energy oxygen vacancy structures. In the sub-figures, the left panel shows the calculated Mulliken up (down) spin population (μ_B) denoted by Green (blue) vector. The right panel shows wavefunction isosurface ($0.05e/\text{Å}^3$) of the localized defect states. The yellow/cyan (green/blue) correspond to positive/negative wavefunction of spin up (down) defect state. (a) the most stable configuration, one spin up excess electron at three nearest neighbor Ce atoms and the other spin down excess electron at next nearest neighbor Ce atom, (b) one spin down excess electron at nearest neighbor two Ce atoms and the other spin up excess electron at nearest neighbor Ce atom, (c) one spin down excess electron at the nearest neighbor Ce atom and the other spin up excess electron at next nearest neighbor Ce atom, (d) one spin up excess electron at the nearest neighbor Ce atom and the other spin down excess electron at next nearest neighbor Ce atom, (e) two excess electrons at nearest neighbor Ce atoms, (f) two excess electrons at next nearest neighbor Ce atoms, and (g) one spin up excess electron at three nearest neighbor Ce atoms and the other spin down excess electron at Ce atom in the middle layer.

found the lowest surface oxygen vacancy formation energy is 0.38 eV in the surface spin polarized system. In contrast, the NSP simulations show higher oxygen vacancy formation energy values: 4.06 eV ($U = 7$ eV) and 3.04 eV ($U = 4$ eV), as compared to several previous reports ranged from 2.13 to 3.20 eV[56,72–74]. Note that two electrons are almost equally populated on two nearest neighbor Ce atoms and one next nearest neighbor Ce in our NSP simulation. In the SP system, the less ionized oxygen ions bond weakly with cerium ions, resulting in lower cost of vacancy formation in comparison to NSP system which does not involve charge transfer process. Therefore, our results indicate that surface spin polarization can lower the oxygen vacancy formation energy, and enhance the oxide reduciblility of the CeO_2-(111) surface.

In addition to the most stable oxygen vacancy defect state, we found several other low-energy spin configurations. In Fig. 2c, local spin moments on two Ce atoms are exchanged in comparison to the most stable configuration in Fig. 2a. This vacancy configuration gives rise to down spin flipping on another nearest neighbor Ce atom and cause an increase in formation energy of 0.2 eV from the most stable oxygen vacancy. In the configuration of Fig. 2b, one electron was equally distributed on two nearest neighbor Ce atoms which have down spin moment of 0.75 μ_B opposite to the majority up surface spin. This configuration leads to increased formation energy of 0.18 eV in comparison to the most stable oxygen vacancy. These indicate that surface spins favor ferromagnetic coupling with excess electrons. In Figure 2d-f, we found very localized defect states with a Mulliken population close to 1.0 μ_B on two Ce atoms. However, that localization does not only weaken ferromagnetic coupling by producing opposite spin moments on the surface, but also increases the repulse Coulomb interaction between excess electrons, resulting in a higher formation energy. In particular, the configuration of Fig. 2f, where two excess electrons are localized on next nearest neighbor Ce atoms, was reported as the most stable oxygen vacancy state by other DFT studies[72,73,75]. However, the configuration is no longer the ground state by considering the spin effect. As shown in Fig. 2g, we also found outstanding oxygen vacancy configuration to be energetically degenerated with the most stable oxygen vacancy configuration. One defect state located on three nearest neighbor Ce atoms increasing spin moment 0.75 μ_B around oxygen vacancy in the ferromagnetic coupling, whereas the other excess electron is moved to the farthest site from surface, which has no spin coupling. In comparison to total spin population on oxygen layer

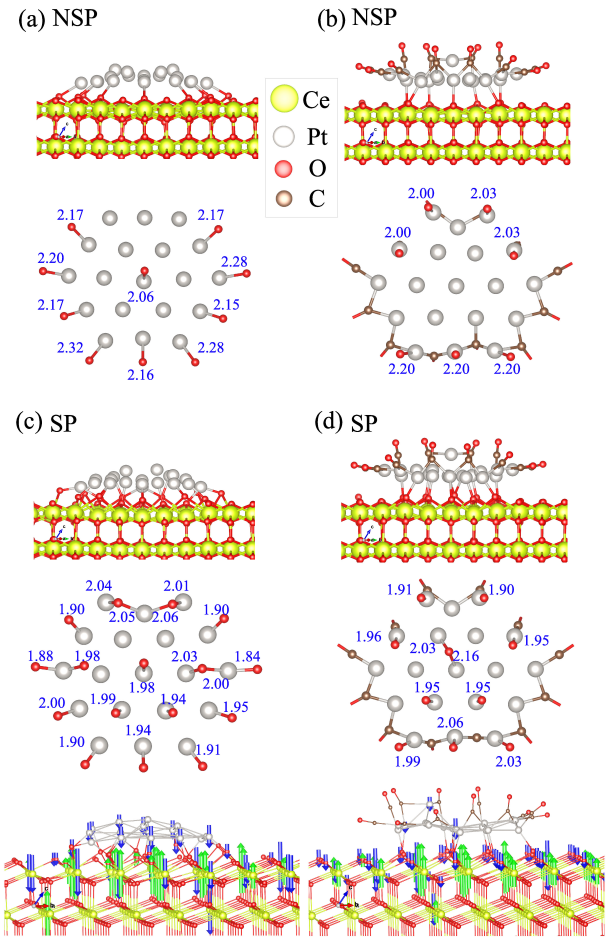

FIG. 3. Optimized Pt single layer on ceria. (a) Pt_{19} single layer on a non-spin polarized CeO_2-(111) surface. (b) $Pt_{19}[CO]_{12}$ on a non-spin polarized CeO_2-(111) surface. (c) Pt_{19} single layer on a spin polarized CeO_2-(111) surface. (d) $Pt_{19}[CO]_{12}$ on a spin polarized CeO_2-(111) surface. The side view of the structures are shown in the top panel. The calculated bond lengths (Å) between Pt and surface oxygen are shown in the middle panel.

of the most stable configuration, this configuration further increased total spin moment of 0.58 (0.39) μ_B on the uppermost (middle) two oxygen layers. This ascertains additional charge transfer to localize the excess electrons. These configurations suggest that even in the presence of oxygen vacancies, there is still surface spin polarization, and it can even be enhanced for some vacancy configurations as shown in Fig. 2.

B. Pt on the ceria support with CO

To date, surface spin polarization has not been taken into account for nano-structured heterogeneous catalysts. Hence we investigated the influence of surface spin polarization on the interaction between Pt nanoparitcle and ceria. As shown in Fig. 3a, the optimized Pt_{19} SL on CeO_2-(111) consisted of platinum and surface oxygen (O_{surf}) bonds mostly on perimeter of the SL in NSP simulation. On the other hand, the SP simulation (see Fig. 3c) generates a configuration with more Pt-O_{surf} bonds. In addition, the averaged bond length is also shorter than that of the NSP configuration. This indicates that the interaction between ceria surface and Pt_{19} SL is significantly enhanced by the surface spin polarization. We attribute the strong Pt-O_{surf} bonds to electron depletion oxygen layer by the charge transfer on the spin polarized surface, where Pt atoms are more prone to oxidation. The enhanced interfacial interaction induces spin moments on Pt and Ce atoms and coupling between them. The surface oxygens were pulled out from ceria surface by this interaction. As a result, the donation of Pt valance electrons to surface oxygens increases the unpaired spin density around the Pt site. The pronounced on-site spin populations on Pt atoms are denoted in Fig. 3c. The interfacial interaction also affects the electronic configuration of Ce atoms on the surface layer. The less oxidized Ce atoms has a large unpaired spin population which couples with the polarized Pt spins through surface oxygen. The majority of magnetic coupling is antiferromagnetic, resulting in a zero net spin moment on the intermediate surface oxygen.

Our simulation shows that adsorption energy of CO on the spin polarized CeO_2-(111) surface is -0.31 eV (see Fig. S1). The result agrees with previous observations that CO on CeO_2-(111) surface is either unstable or has weak interaction with the surface[76–78] (see Section B in the SI). In terms of CO's adsorption energy on the ceria-supported Pt nanoparticle, our calculation reveals a wide distribution from -3.14 to -1.02 eV, depending on the choice of adsorption sites (see Fig. S2). These results indicate that CO molecules are strongly adsorbed on Pt nanoparicles[79]. In this work, we constructed ceria-supported Pt_{19} SL with 12 CO molecules which were initially located at the bridging sites of the perimeter of Pt_{19}. Optimized geometries of $Pt_{19}[CO]_{12}$ with/without surface spin polarization are shown in Fig. 3b and d. We again observed that surface spin polarization enhances the interaction between $Pt_{19}[CO]_{12}$ and ceria, i.e., more bonds and shorter bond lengths.

Fig. 3 shows that the CO adsorption on Pt_{19} breaks a few Pt-O_{surf} bonds on the perimeter of Pt_{19} in both NSP and SP calculations. Thus, the adsorption weakens the interfacial interaction. The weakening can be understood from Mulliken spin population analysis in the SP system. The strong CO adsorption on Pt_{19}, due to the π-back bonding between Pt and CO[80], can reduce the donation of Pt's valence electron to surface oxygen. As a result, the pairing electrons on Pt atoms decreases the net spin moment on the Pt_{19} (see Figure 3c-d).

C. Reaction pathway in CO oxidation

We found that surface spin polarization may play an important role in the catalytic activity. On a spin polarized surface, the electrophilic oxygens in the electron deficient condition are more reactive with other species in comparison to the NSP system. In addition, new species formed by the reaction are easily removable owing to the high reducibility on the spin polarized surface. The impact of spin polarization on surface

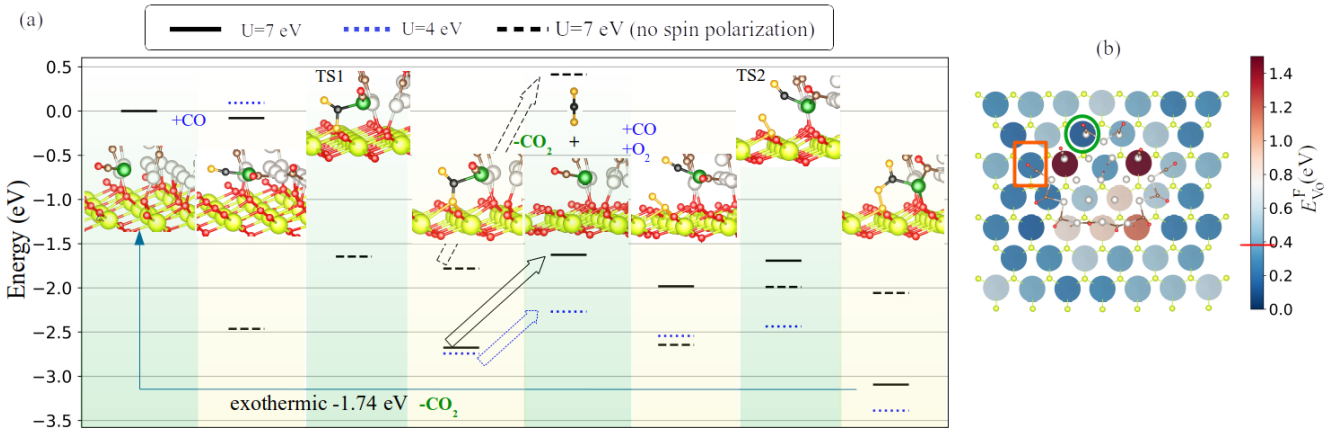

FIG. 4. (a) The calculated energy profiles for proposed reaction pathway for CO oxidation on $Pt_{19}[CO]_{11}$ with the ceria support. The black solid (blue dotted) lines show the calculated energy profiles by using U = 7.0 (4.0) eV from the spin polarized simulations. The black dashed lines show the calculated energy profiles by using U = 7.0 eV from the non-spin polarized simulations. TS1 and TS2 denote two transition states. CO is absorbed on green colored Pt atom. C (O) atoms involved in the reaction were colored by black (yellow). (b) Calculated surface oxygen vacancy formation energies within SP simulations. Filled circles represent the formation energies at corresponding sites. The surface oxygen which react with CO was marked by the red box. The surface oxygen with exceptional low vacancy formation energy was marked by the green circle. The energy level of oxygen vacancy formation for the most stable configuration on bare ceria surface is marked by red line on the energy color bar.

TABLE II. The list of activation barriers in energy profiles for proposed reaction pathway. The major activation barriers are hilighted in bold.

Calculation Type	Parameter	Reaction Barrier (eV)		
	U (eV)	TS1	-CO_2	TS2
Spin Polarization	7.0	0	**1.05**	0.29
Spin Polarization	4.0	0	**0.47**	0.11
Non-spin Polarization	7.0	0.82	**2.19**	0.65

catalytic activity is illustrated in Fig. 4a. We started with a CO desorpted $Pt_{19}[CO]_{11}$ with ceria support in CO rich conditions. The $Pt_{19}[CO]_{11}$ can adsorb one more CO molecule to form $Pt_{19}[CO]_{12}$, with a shallow adsorption energy of -0.08 eV. The adsorbed CO reacts with O_{surf} to form CO_2, gaining an energy of 2.60 eV. While there is no activation barrier for the reaction in the SP system, calculated activation barrier is 0.82 eV in the NSP system. Taking off the CO_2 molecule from the reaction site leaves a surface oxygen vacancy, costing an penalty energy of 1.05 eV for U = 7 eV (0.47 eV for U = 4 eV). This is the main barrier in the proposed reaction pathway**.** The Pt SL can subsequently adsorb another incoming CO, while the ceria surface can attract O_2 at the oxygen vacancy site. The molecular O_2 and CO further react to form a new CO_2. The calculated activation barrier for the reaction are 0.29 (U = 7 in the SP system), 0.11 (U = 4 in SP system), and 0.65 (U = 7 in the NSP system) eV, respectively. Thereafter, the catalytic cycle is completed by desorption of the CO_2, which is an exothermic process releasing energy of 1.74 eV to recover to $Pt_{19}[CO]_{11}$. This proposed reaction pathway is manifested by MvK mechanism[7]. The simulated reaction pathway using U = 4 eV has the same trend with U = 7 eV, as shown in Fig. 4a. However, the NSP system shows different reaction energy profiles from the SP system. Table. II summarizes the activation barriers for each system. The major activation barriers (0.47-1.05 eV) of the SP system are apparently close to the measured activation energies ranging from 0.37 to 0.77 eV[36,79,81–83], while the NSP system has a much higher barrier (2.19 eV). The elevated barrier in the NSP system is caused by high formation energy of oxygen vacancy, that hampers the release of CO_2 from the surface.

In addition to lowering the activation barrier, the surface spin polarization enables the adsorbed CO on Pt SL to react with O_{surf} to form CO_2. While this reaction is endothermic in the NSP system, the energy released by the reaction is large in the SP system, owing to high surface oxygen reactivity. Compared to the most stable oxygen vacancy on a bare ceria surface, the surface oxygen (at the reaction site marked by red box in Fig. 4b) vacancy formation energy with $Pt_{19}[CO]_{12}$ is lowered by 0.15 eV, thus significantly boosting the reaction with surface oxygen. In Fig. 4b, we show the calculated vacancy formation energies for all surface oxygen sites. The interaction between $Pt_{19}[CO]_{12}$ and CeO_2 generally lowers the vacancy formation energies for surface oxygen at exterior sites of the contact zone. However, within the contact zone, the majority of surface oxygens strongly bond with Pt ions (see Fig. 3d). The vacancy formation energies are relatively high for these oxygen, except the oxygen which bonds with Pt-CO (marked by green circle in Fig. 5b). The O_{surf}-Pt-CO at the exceptional site may migrate by forming dynamic low-coordinated atoms, which has been proposed as the prime cause of dynamic structure of ceria supported gold nanoparticles upon exposing to CO and oxygen gases[43]. The impact of surface spin polarization on structural dynamics will be discussed in the following section.

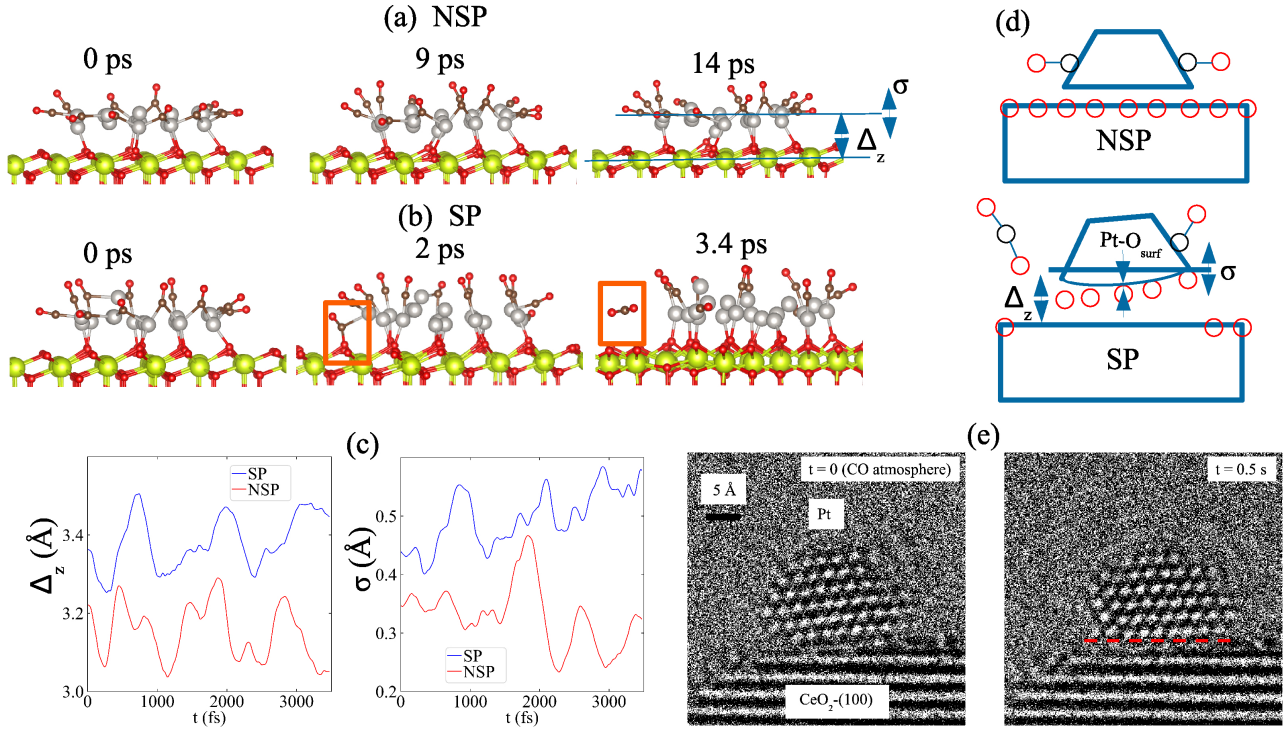

FIG. 5. (a) The snap shot of NSP AIMD simulation of the ceria-supported Pt_{19} single layer with 12 CO molecules at 0, 9 and 14 ps. (b) The snap shot of SP AIMD simulation of the ceria-supported Pt_{19} single layer with 12 CO molecules at 0, 2 and 3.4 ps. The red box shows that the CO and surface O bind to form CO_2. (c) Left panel: calculated distance between the average z coordinates of surface Ce atoms and the average z coordinates of Pt atoms, right panel: standard deviation of z coordinates of Pt atoms. (d) Schematic diagram of lattice dynamic in SP and NSP systems. (e) Atomic resolution transmission electron microscope images of fluxional Pt nanoparticle on CeO_2-(100) surface in a CO atmosphere (7×10^{-4} Torr) at room temperature. Pt columns are visible as white dots whereas (100) Miller planes in CeO_2 appear as white horizonal lines. The two images are from the same nanoparticle with right-hand image recorded 0.5s after the left-hand image. The Pt nanoparticles undergoes 7.5° clockwise rotation resulting in Pt (111) becoming approximately parallel to (100) CeO_2 plane (see red dotted guide to eye on right-hand panel). The Pt atomic plane near the CeO_2 is not straight and curves up on left-hand side and also the atomic columns on the right are slightly blurred suggesting a high degree of instability in their position. Other changes in the Pt surface structure are apparent due to the strong interaction with CO.

D. Structural dynamics

The dynamic lattice reconfiguration of nanoparticles upon exposing to oxidizing and reducing gases (e.g. CO and O_2) has been intensively studied by Transmission Electron Microscopy (TEM) in the recent years[34–36,43,84–92]. These studies imply that the surface and perimeter of nanoparticle strongly interact with CO and O_2 gases. To explore the potential influence of surface spin polarization on the dynamic lattice reconfiguration, we performed two independent AIMD simulations of ceria-supported Pt nanoparticles for 20 ps with and without the inclusion of spin polarization. Due to the limitation of computational resources, we used only three layers of O-Ce-O. Therefore, the CeO_2 support is highly reducible, resulting in a unrealistically fast CO oxidation even at 300 K in our AIMD simulation.

Despite the artefact due to the choice of a thin CeO_2 slab, our simulations still reveal distinct physical pictures due to the inclusion of spin polarization. In the NSP AIMD simulation (Fig. 5a), the whole system does not show any obvious structural change for 20 ps. On the other hand, we observed rapid CO_2 formation at around 3 ps (Fig. 5b) when the spin polarization is turned on. Fig. 5c plots the calculated distance between the averaged z coordinates of surface Ce/Pt atoms, as well as the standard deviation to evaluate dispersion of z coordinates of Pt atoms during the simulation. Clearly, the Pt atoms in the SP system are more distant from surface Ce atoms with a larger fluctuation, in comparison to the NSP system. Accordingly, we identify four different features of the SP system (in schematic Fig. 5d). First, strong bonds between Pt and surface oxygen atoms are found in the SP system. This is shown by more bonds and shorter bond lengths because oxygen has moved towards the Pt layer as seen in Fig. 3. Second, the large distances between surface Ce and Pt atoms are present consistently in the SP AIMD simulations. Highly reducible surface oxygen in the SP surface bond strongly with Pt atoms, resulting in an elevation of surface oxygen and Pt atoms from CeO_2 surface. This shifting is also manifested in the optimized structures in Fig. 3. Third, substantial fluctuations of Pt atoms are displayed in the SP AIMD simulations, indicating that the elevated Pt nanoparticle from CeO_2 surface

are flexible. Fourth, asymmetric CO oxidation was raised by irregular structure of Pt and nonuniform surface O vacancy formation energies as shown in Fig. 4b.

Recently, experimental evidence has been published that shows significant lattice reconfiguration on Pt nanoparticles supported on CeO_2 on exposure to CO and other gases[35,36,92] While the timescales for the computation and experimental datasets are very different, precluding a detailed quantitative structural comparison, there is qualitative agreement in the trends in structural dynamics from both theory and experiment. Fig. 5e is in situ electron microscopy data showing dynamic structural change taking place in a CO atmosphere (for experimental details see reference[92]). The Pt nanoparticles undergoes complex lattice changes such as clockwise rotation, uneven Pt atomic plane near the CeO_2, instability its atomic position, and apparent change on the Pt surface. There are also continuing changes in the interface structure due to the constant creation and annihilation of oxygen vacancies at perimeter sites. This occurs due to the weakening of the interfacial bonds in the presence of CO and the experimental observation can be understood in terms of the schematic diagram of Fig. 5d. There are many other fluxional observations such as dynamic changes in cation positions due to breaking and formation of chemical bonds at the perimeter sites which are described in greater detail in the author's paper[36] . These complex dynamics may be described by concerted effect from aforementioned four features, which are pronounced in our SP AIMD simulation. Thus, we suggest that surface spin polarization may play a deterministic role in promoting the dynamic lattice reconfiguration of ceria-supported Pt nanoparticles.

IV. CONCLUSIONS

In summary, we report the robust surface spin polarization on the CeO_2-(111) surface due to charge transfer from surface oxygen to cerium. The surface spin polarization appears to be essential to describe the existing important observations such as ferromagnetism in undoped CeO_2 nanostructures and thin films, high reducibility of ceria support, and low CO oxidation reaction barrier. In addition, the surface spin polarization enhances the bonding between platinum and surface oxygen. However, the CO adsorption on the perimeter of platinum single layer is inclined to weaken the interfacial interaction. We expect the presence of vigorous surface spin polarization at ambient temperature will be useful to understand the interfacial interaction and guide the design high-performance heterogeneous catalyst.

ACKNOWLEDGMENTS

The computing resources are provided by XSEDE (TG-DMR180040). The authors gratefully acknowledge financial support from the National Science Foundation (NSF). BK and QZ are supported by NSF-OAC award 1940272. NSF-CBET Award 1604971 and NSF-OAC Award 1940263 supported JLV and PAC, who acquired and processed the experimental data and participated in extensive discussion of the calculations. The authors thank Arizona State University's John M. Cowley Center for High Resolution Electron Microscopy for microscope access and use.

[1] P. C. Stair, "Where the action is," Nat. Chem. **3**, 345–346 (2011).
[2] Y. Yamada, C.-K. Tsung, W. Huang, Z. Huo, S. E. Habas, T. Soejima, C. E. Aliaga, G. A. Somorjai, and P. Yang, "Nanocrystal bilayer for tandem catalysis," Nat. Chem. **3**, 372–376 (2011).
[3] J. Zhang, H. Wang, L. Wang, S. Ali, C. Wang, L. Wang, X. Meng, B. Li, D. S. Su, and F.-S. Xiao, "Wet-chemistry strong metal–support interactions in titania-supported au catalysts," J. Am. Chem. Soc. **141**, 2975–2983 (2019).
[4] S. Song, Y. Wu, S. Ge, L. Wang, Y. Wang, Y. Guo, W. Zhan, and Y. Guo, "A facile way to improve pt atom efficiency for co oxidation at low temperature: modification by transition metal oxides," ACS Catal. **9**, 6177–6187 (2019).
[5] H. Zhu, Z. Wu, D. Su, G. M. Veith, H. Lu, P. Zhang, S.-H. Chai, and S. Dai, "Constructing hierarchical interfaces: Tio_2-supported ptfe–feo_x nanowires for room temperature co oxidation," J. Am. Chem. Soc. **137**, 10156–10159 (2015).
[6] Y. Fang, X. Chi, L. Li, J. Yang, S. Liu, X. Lu, W. Xiao, L. Wang, Z. Luo, W. Yang, *et al.*, "Elucidating the nature of the cu (i) active site in cuo/tio_2 for excellent low-temperature co oxidation," ACS Appl. Mater. Interfaces **12**, 7091–7101 (2020).
[7] P. Mars and D. W. Van Krevelen, "Oxidations carried out by means of vanadium oxide catalysts," Chem. Eng. Sci. **3**, 41–59 (1954).
[8] S. Tauster, S. Fung, and R. L. Garten, "Strong metal-support interactions. group 8 noble metals supported on titanium dioxide," J. Am. Chem. Soc. **100**, 170–175 (1978).
[9] S. Tauster, S. Fung, R. Baker, and J. Horsley, "Strong interactions in supported-metal catalysts," Science **211**, 1121–1125 (1981).
[10] S. Tauster, "Strong metal-support interactions," Acc. Chem. Res. **20**, 389–394 (1987).
[11] H. Tang, Y. Su, B. Zhang, A. F. Lee, M. A. Isaacs, K. Wilson, L. Li, Y. Ren, J. Huang, M. Haruta, *et al.*, "Classical strong metal–support interactions between gold nanoparticles and titanium dioxide," Sci. Adv. **3**, e1700231 (2017).
[12] H. Wang, L. Wang, D. Lin, X. Feng, Y. Niu, B. Zhang, and F.-S. Xiao, "Strong metal–support interactions on gold nanoparticle catalysts achieved through le chatelier's principle," Nat. Catal. **4**, 418–424 (2021).
[13] G. Pacchioni and H.-J. Freund, "Controlling the charge state of supported nanoparticles in catalysis: lessons from model systems," Chem. Soc. Rev. **47**, 8474–8502 (2018).
[14] C. T. Campbell, "Electronic perturbations," Nat. Chem. **4**, 597–598 (2012).
[15] G. Pacchioni, "Electronic interactions and charge transfers of metal atoms and clusters on oxide surfaces," Phys. Chem. Chem. Phys. **15**, 1737–1757 (2013).
[16] I. Ro, J. Resasco, and P. Christopher, "Approaches for understanding and controlling interfacial effects in oxide-supported metal catalysts," ACS Catal. **8**, 7368–7387 (2018).
[17] M. Haruta, "Size-and support-dependency in the catalysis of gold," Catal. Today **36**, 153–166 (1997).
[18] A. Boubnov, S. Dahl, E. Johnson, A. P. Molina, S. B. Simonsen, F. M. Cano, S. Helveg, L. J. Lemus-Yegres, and J.-D. Grunwaldt, "Structure–activity relationships of pt/al_2o_3 catalysts for co and no oxidation at diesel exhaust conditions," Appl. Catal., B **126**, 315–325 (2012).
[19] J. Liu, "Catalysis by supported single metal atoms," Acs Catal. **7**, 34–59 (2017).
[20] A. Ruiz Puigdollers, P. Schlexer, S. Tosoni, and G. Pacchioni, "Increasing oxide reducibility: the role of metal/oxide interfaces in the formation of oxygen vacancies," ACS Catal. **7**, 6493–6513 (2017).
[21] Y.-G. Wang, Y. Yoon, V.-A. Glezakou, J. Li, and R. Rousseau, "The role of reducible oxide–metal cluster charge transfer in catalytic processes: new insights on the catalytic mechanism of co oxidation on au/tio_2 from ab initio molecular dynamics," J. Am. Chem. Soc. **135**, 10673–10683 (2013).
[22] H.-H. Liu, Y. Wang, A.-P. Jia, S.-Y. Wang, M.-F. Luo, and J.-Q. Lu, "Oxygen vacancy promoted co oxidation over pt/ceo_2 catalysts: A reaction at pt–ceo_2 interface," Applied Surf. Sci. **314**, 725–734 (2014).

[23] K. Liu, A. Wang, and T. Zhang, "Recent advances in preferential oxidation of co reaction over platinum group metal catalysts," ACS Catal. **2**, 1165–1178 (2012).

[24] D. Widmann and R. J. Behm, "Active oxygen on a au/tio$_2$ catalyst: formation, stability, and co oxidation activity," Angew. Chem. Int. Ed. **50**, 10241–10245 (2011).

[25] H. Y. Kim, H. M. Lee, and G. Henkelman, "Co oxidation mechanism on ceo$_2$-supported au nanoparticles," J. Am. Chem. Soc. **134**, 1560–1570 (2012).

[26] G. N. Vayssilov, Y. Lykhach, A. Migani, T. Staudt, G. P. Petrova, N. Tsud, T. Skála, A. Bruix, F. Illas, K. C. Prince, *et al.*, "Support nanostructure boosts oxygen transfer to catalytically active platinum nanoparticles," Nat. Mater. **10**, 310–315 (2011).

[27] G. A. Somorjai, "The flexible surface. correlation between reactivity and restructuring ability," Langmuir **7**, 3176–3182 (1991).

[28] R. Imbihl and G. Ertl, "Oscillatory kinetics in heterogeneous catalysis," Chem. Rev. **95**, 697–733 (1995).

[29] G. Ertl, "Reactions at surfaces: From atoms to complexity (nobel lecture)," Angew. Chem. Int. Ed. **47**, 3524–3535 (2008).

[30] F. Cotton, "Fluxionality in organometallics and metal carbonyls," Journal of Organometallic Chemistry **100**, 29–41 (1975).

[31] Z. Zhang, B. Zandkarimi, and A. N. Alexandrova, "Ensembles of metastable states govern heterogeneous catalysis on dynamic interfaces," Acc. Chem. Res. **53**, 447–458 (2020).

[32] G. Sun and P. Sautet, "Metastable structures in cluster catalysis from first-principles: Structural ensemble in reaction conditions and metastability triggered reactivity," J. Am. Chem. Soc. **140**, 2812–2820 (2018).

[33] H. Zhai and A. N. Alexandrova, "Fluxionality of catalytic clusters: When it matters and how to address it," ACS Catal. (2017), 10.1021/acscatal.6b03243.

[34] E. L. Lawrence, B. D. Levin, T. Boland, S. L. Chang, and P. A. Crozier, "Atomic scale characterization of fluxional cation behavior on nanoparticle surfaces: Probing oxygen vacancy creation/annihilation at surface sites," ACS nano **15**, 2624–2634 (2021).

[35] Y. Li, M. Kottwitz, J. L. Vincent, M. J. Enright, Z. Liu, L. Zhang, J. Huang, S. D. Senanayake, W.-C. D. Yang, P. A. Crozier, *et al.*, "Dynamic structure of active sites in ceria-supported pt catalysts for the water gas shift reaction," Nat. Comm. **12**, 1–9 (2021).

[36] J. L. Vincent and P. A. Crozier, "Fluxional behavior at the atomic level and its impact on activity: Co oxidation over ceo -{2}-supported pt catalysts," arXiv preprint arXiv:2104.00821 (2021), arXiv:2104.00821.

[37] K. Ackland and J. Coey, "Room temperature magnetism in ceo$_2$—a review," Phys. Rep. **746**, 1–39 (2018).

[38] C. Artini, M. Pani, M. M. Carnasciali, M. T. Buscaglia, J. R. Plaisier, and G. A. Costa, "Structural features of sm-and gd-doped ceria studied by synchrotron x-ray diffraction and μ-raman spectroscopy," Inorg. Chem. **54**, 4126–4137 (2015).

[39] J. VandeVondele, M. Krack, F. Mohamed, M. Parrinello, T. Chassaing, and J. Hutter, "Quickstep: Fast and accurate density functional calculations using a mixed gaussian and plane waves approach," Comput. Phys. Commun. **167**, 103–128 (2005).

[40] S. Goedecker, M. Teter, and J. Hutter, "Separable dual-space gaussian pseudopotentials," Phys. Rev. B **54**, 1703 (1996).

[41] J. P. Perdew, K. Burke, and M. Ernzerhof, "Generalized gradient approximation made simple," Phys. Rev. Lett. **77**, 3865 (1996).

[42] S. Grimme, J. Antony, S. Ehrlich, and H. Krieg, "A consistent and accurate ab initio parametrization of density functional dispersion correction (dft-d) for the 94 elements h-pu," J. Chem. Phys. **132**, 154104 (2010).

[43] Y. He, J.-C. Liu, L. Luo, Y.-G. Wang, J. Zhu, Y. Du, J. Li, S. X. Mao, and C. Wang, "Size-dependent dynamic structures of supported gold nanoparticles in co oxidation reaction condition," Proc. Natl. Acad. Sci. U.S.A. **115**, 7700–7705 (2018).

[44] Y.-G. Wang, D. Mei, V.-A. Glezakou, J. Li, and R. Rousseau, "Dynamic formation of single-atom catalytic active sites on ceria-supported gold nanoparticles," Nat. Commun. **6**, 1–8 (2015).

[45] G. Henkelman, B. P. Uberuaga, and H. Jónsson, "A climbing image nudged elastic band method for finding saddle points and minimum energy paths," J. Chem. Phys. **113**, 9901–9904 (2000).

[46] G. Xiao, Z. Xia, M. Wei, S. Huang, L. Shi, X. Zhang, H. Wu, F. Yang, Y. Song, and Z. Ouyang, "Modulation of jahn-teller effect on magnetization and spontaneous electric polarization of cufeo$_2$," J. Magn. Magn. Mater. **449**, 214–222 (2018).

[47] R. Pentcheva, F. Wendler, H. L. Meyerheim, W. Moritz, N. Jedrecy, and M. Scheffler, "Jahn-teller stabilization of a "polar" metal oxide surface: Fe$_3$o$_4$ (001)," Phys. Rev. Lett. **94**, 126101 (2005).

[48] Y. Kurtulus and R. Dronskowski, "Electronic structure, chemical bonding, and spin polarization in ferromagnetic mnal," J. Solid State Chem. **176**, 390–399 (2003).

[49] A. Zywietz, J. Furthmüller, and F. Bechstedt, "Spin state of vacancies: From magnetic jahn-teller distortions to multiplets," Phys. Rev. B **62**, 6854 (2000).

[50] M. Anwar, S. Kumar, F. Ahmed, N. Arshi, G.-S. Kil, D.-W. Park, J. Chang, and B. H. Koo, "Hydrothermal synthesis and indication of room temperature ferromagnetism in ceo$_2$ nanowires," Mater. Lett. **65**, 3098–3101 (2011).

[51] M. Li, S. Ge, W. Qiao, L. Zhang, Y. Zuo, and S. Yan, "Relationship between the surface chemical states and magnetic properties of ceo$_2$ nanoparticles," Appl. Phys. Lett. **94**, 152511 (2009).

[52] N. Paunović, Z. Dohčević-Mitrović, R. Scurtu, S. Aškrabić, M. Prekajski, B. Matović, and Z. V. Popović, "Suppression of inherent ferromagnetism in pr-doped ceo$_2$ nanocrystals," Nanoscale **4**, 5469–5476 (2012).

[53] S. Phokha, E. Swatsitang, and S. Maensiri, "Room-temperature ferromagnetism in pure ceo$_2$ nanoparticles prepared by a simple direct thermal decomposition," Electronic Mater. Lett. **11**, 1012–1020 (2015).

[54] A. Sundaresan and C. Rao, "Ferromagnetism as a universal feature of inorganic nanoparticles," Nano Today **4**, 96–106 (2009).

[55] Y. Liu, Z. Lockman, A. Aziz, and J. MacManus-Driscoll, "Size dependent ferromagnetism in cerium oxide (ceo$_2$) nanostructures independent of oxygen vacancies," J. Phys.: Condens. Matter. **20**, 165201 (2008).

[56] M. Li, R. Zhang, H. Zhang, W. Feng, and X. Liu, "Synthesis, structural and magnetic properties of ceo$_2$ nanoparticles," Micro Nano Lett. **5**, 95–99 (2010).

[57] V. Fernandes, P. Schio, R. Mossanek, A. De Oliveira, W. Ortiz, D. Demaille, F. Vidal, Y. Zheng, P. Fichtner, L. Amaral, *et al.*, "Anisotropy of magnetization and nanocrystalline texture in electrodeposited ceo$_2$ films," Electrochem. Solid-State Lett. **14**, P9 (2010).

[58] V. Fernandes, P. Schio, A. De Oliveira, W. Ortiz, P. Fichtner, L. Amaral, I. Graff, J. Varalda, N. Mattoso, W. Schreiner, *et al.*, "Ferromagnetism induced by oxygen and cerium vacancies above the percolation limit in ceo$_2$," J. Phys.: Condens. Matter. **22**, 216004 (2010).

[59] V. Fernandes, R. Mossanek, P. Schio, J. Klein, A. De Oliveira, W. Ortiz, N. Mattoso, J. Varalda, W. Schreiner, M. Abbate, *et al.*, "Dilute-defect magnetism: Origin of magnetism in nanocrystalline ceo$_2$," Phys. Rev. B **80**, 035202 (2009).

[60] G.-R. Li, D.-L. Qu, X.-L. Yu, and Y.-X. Tong, "Microstructural evolution of ceo$_2$ from porous structures to clusters of nanosheet arrays assisted by gas bubbles via electrodeposition," Langmuir **24**, 4254–4259 (2008).

[61] N. Figueiredo-Prestes, J. Zarpellon, H. F. Jurca, V. Fernandes, J. Varalda, *et al.*, "Stabilization of perpendicular magnetic anisotropy in ceo$_2$ films deposited on co/pt multilayers," RSC Adv. **6**, 56785–56789 (2016).

[62] M. Ge, H. Wang, E. Liu, J. Liu, J. Jiang, Y. Li, Z. Xu, and H. Li, "On the origin of ferromagnetism in ceo$_2$ nanocubes," Appl. Phys. Lett. **93**, 062505 (2008).

[63] A. El Hachimi, H. Zaari, M. Boujnah, A. Benyoussef, M. El Yadari, and A. El Kenz, "Ferromagnetism induced by oxygen related defects in ceo$_2$ from first principles study," Comput. Mater. Sci. **85**, 134–137 (2014).

[64] P. R. Keating, D. O. Scanlon, B. J. Morgan, N. M. Galea, and G. W. Watson, "Analysis of intrinsic defects in ceo$_2$ using a koopmans-like gga+ u approach," J. Phys. Chem. C **116**, 2443–2452 (2012).

[65] A. N. Ribeiro and N. d. S. Ferreira, "Systematic study of the physical origin of ferromagnetism in ceo$_2$- δ nanoparticles," Phys. Rev. B **95**, 144430 (2017).

[66] X. Han, N. Amrane, Z. Zhang, and M. Benkraouda, "Oxygen vacancy ordering and electron localization in ceo$_2$: hybrid functional study," J. Phys. Chem. C **120**, 13325–13331 (2016).

[67] X. Han, J. Lee, and H.-I. Yoo, "Oxygen-vacancy-induced ferromagnetism in ceo$_2$ from first principles," Phys. Rev. B **79**, 100403 (2009).

[68] R. A. Ribeiro, J. Andrés, E. Longo, and S. R. Lazaro, "Magnetism and multiferroic properties at mntio$_3$ surfaces: A dft study," Applied Surf. Sci. **452**, 463–472 (2018).

[69] A. H. Hashim, S. M. Zain, V. S. Lee, S. M. Said, *et al.*, "Electronic, magnetic and structural properties of co3o$_4$ (100) surface: a dft+ u study," Applied Surf. Sci. **427**, 1090–1095 (2018).

[70] M. C. Munoz, S. Gallego, and N. Sanchez, "Surface ferromagnetism in non-magnetic and dilute magnetic oxides," J. Phys. Conf. Ser. **303**, 012001 (2011).

[71] S. Hayun, S. V. Ushakov, and A. Navrotsky, "Direct measurement of surface energy of ceo$_2$ by differential scanning calorimetry," J. Am. Ceram. Soc. **94**, 3679–3682 (2011).

[72] Y.-L. Song, L.-L. Yin, J. Zhang, P. Hu, X.-Q. Gong, and G. Lu, "A dft+ u study of co oxidation at ceo$_2$ (110) and (111) surfaces with oxygen vacancies," Surf. Sci. **618**, 140–147 (2013).

[73] H.-Y. Li, H.-F. Wang, X.-Q. Gong, Y.-L. Guo, Y. Guo, G. Lu, and P. Hu, "Multiple configurations of the two excess 4 f electrons on defective ceo$_2$ (111): origin and implications," Phys. Rev. B **79**, 193401 (2009).

[74] M. V. Ganduglia-Pirovano, J. L. Da Silva, and J. Sauer, "Density-functional calculations of the structure of near-surface oxygen vacancies and electron localization on ceo$_2$ (111)," Phys. Rev. Lett. **102**, 026101 (2009).

[75] Z.-K. Han, Y.-Z. Yang, B. Zhu, M. V. Ganduglia-Pirovano, and Y. Gao, "Unraveling the oxygen vacancy structures at the reduced ceo$_2$ (111) surface," Phys. Rev. Mater. **2**, 035802 (2018).

[76] F. Chen, D. Liu, J. Zhang, P. Hu, X.-Q. Gong, and G. Lu, "A dft+ u study of the lattice oxygen reactivity toward direct co oxidation on the ceo$_2$ (111) and (110) surfaces," Phys. Chem. Chem. Phys. **14**, 16573–16580 (2012).

[77] M. Huang and S. Fabris, "Co adsorption and oxidation on ceria surfaces from dft+ u calculations," J. Phys. Chem. C **112**, 8643–8648 (2008).

[78] M. Nolan and G. W. Watson, "The surface dependence of co adsorption on ceria," J. Phys. Chem. B **110**, 16600–16606 (2006).

[79] Y. Lu, C. Thompson, D. Kunwar, A. K. Datye, and A. M. Karim, "Origin of the high co oxidation activity on ceo$_2$ supported pt nanoparticles: weaker binding of co or facile oxygen transfer from the support?" ChemCatChem **12**, 1726–1733 (2020).

[80] S. Das, K. Dutta, Y. G. Shul, and P. P. Kundu, "Progress in developments of inorganic nanocatalysts for application in direct methanol fuel cells," Crit. Rev. Solid State Mater. Sci. **40**, 316–357 (2015).

[81] J. Ke, W. Zhu, Y. Jiang, R. Si, Y.-J. Wang, S.-C. Li, C. Jin, H. Liu, W.-G. Song, C.-H. Yan, *et al.*, "Strong local coordination structure effects on subnanometer pto$_x$ clusters over ceo$_2$ nanowires probed by low-temperature co oxidation," ACS Catal. **5**, 5164–5173 (2015).

[82] M. Cargnello, V. V. Doan-Nguyen, T. R. Gordon, R. E. Diaz, E. A. Stach, R. J. Gorte, P. Fornasiero, and C. B. Murray, "Control of metal nanocrystal size reveals metal-support interface role for ceria catalysts," Science **341**, 771–773 (2013).

[83] R. Kopelent, J. A. van Bokhoven, J. Szlachetko, J. Edebeli, C. Paun, M. Nachtegaal, and O. V. Safonova, "Catalytically active and spectator ce^{3+} in ceria-supported metal catalysts," Angew. Chem. **127**, 8852–8855 (2015).

[84] P. L. Hansen, J. B. Wagner, S. Helveg, J. R. Rostrup-Nielsen, B. S. Clausen, and H. Topsøe, "Atom-resolved imaging of dynamic shape changes in supported copper nanocrystals," Science **295**, 2053–2055 (2002).

[85] Y. Nagai, K. Dohmae, Y. Ikeda, N. Takagi, T. Tanabe, N. Hara, G. Guilera, S. Pascarelli, M. A. Newton, O. Kuno, *et al.*, "In situ redispersion of platinum autoexhaust catalysts: an on-line approach to increasing catalyst lifetimes?" Angew. Chem. Int. Ed. **47**, 9303–9306 (2008).

[86] S. Vendelbo, C. F. Elkjær, H. Falsig, I. Puspitasari, P. Dona, L. Mele, B. Morana, B. Nelissen, R. Van Rijn, J. Creemer, *et al.*, "Visualization of oscillatory behaviour of pt nanoparticles catalysing co oxidation," Nat. Mater. **13**, 884–890 (2014).

[87] A. M. Gänzler, M. Casapu, A. Boubnov, O. Müller, S. Conrad, H. Lichtenberg, R. Frahm, and J.-D. Grunwaldt, "Operando spatially and time-resolved x-ray absorption spectroscopy and infrared thermography during oscillatory co oxidation," J. Catal. **328**, 216–224 (2015).

[88] A. M. Gänzler, M. Casapu, P. Vernoux, S. Loridant, F. J. Cadete Santos Aires, T. Epicier, B. Betz, R. Hoyer, and J.-D. Grunwaldt, "Tuning the structure of platinum particles on ceria in situ for enhancing the catalytic performance of exhaust gas catalysts," Angew. Chem. Int. Ed. **56**, 13078–13082 (2017).

[89] E. L. Lawrence and P. A. Crozier, "Oxygen transfer at metal-reducible oxide nanocatalyst interfaces: Contrasting carbon growth from ethane and ethylene," ACS Applied Nano Materials **1**, 1360–1369 (2018).

[90] B. K. Miller and P. A. Crozier, "Linking changes in reaction kinetics and atomic-level surface structures on a supported ru catalyst for co oxidation," ACS Catal. **11**, 1456–1463 (2021).

[91] F. Tao and P. A. Crozier, "Atomic-scale observations of catalyst structures under reaction conditions and during catalysis," Chem. Rev. **116**, 3487–3539 (2016).

[92] J. Vincent and P. Crozier, "Atomic-resolution operando and time-resolved in situ tem imaging of oxygen transfer reactions catalyzed by ceo$_2$-supported pt nanoparticles," Microscopy and Microanalysis **26**, 1694–1695 (2020).